4534 *Inorg. Chem.* **2001,** *40,* 4534−4542

Green and Red Light Emission by Upconversion from the near-IR in Yb^{3+} Doped $CsMnBr_3$

Pascal Gerner, Oliver S. Wenger, Rafael Valiente, and Hans U. Güdel*

Department of Chemistry and Biochemistry, Freiestrasse 3, CH-3000 Bern 9, Switzerland

Received January 22, 2001

Direct near-IR excitation of Yb^{3+} $^2F_{7/2} \rightarrow {}^2F_{5/2}$ levels at 10126, 10138, and 10596 cm^{-1} in $CsMnBr_3$:0.5%Yb^{3+} leads to three types of luminescence at cryogenic temperatures: near-IR Yb^{3+} emission and green and red upconverted luminescence. The green luminescence around 20 000 cm^{-1} is identified as cooperative Yb^{3+} pair upconversion. The broad red upconversion luminescence band centered at 14 700 cm^{-1} is ascribed to the $^4T_{1g} \rightarrow {}^6A_{1g}$ transition of Mn^{2+}. Pulsed measurements indicate a sequence of ground-state absorption and excited-state absorption steps for the red upconversion process. One- and two-color excitation experiments support this, and we conclude that the red upconversion occurs by an exchange mechanism involving Yb^{3+} and Mn^{2+}. The Yb^{3+} $^2F_{5/2} \rightarrow {}^2F_{7/2}$ near-IR emission around 10 000 cm^{-1} is also observed after Mn^{2+} excitation at 21 838 cm^{-1}. This is indicative of a Mn^{2+} $^4T_{1g} \rightarrow$ Yb^{3+} $^2F_{5/2}$ relaxation process, which is a potential loss process for upconversion efficiency.

1. Introduction

Upconversion (UC) processes provide an efficient way to combine photons of low energy to photons of higher energy. Various mechanisms leading to UC have been discovered and established since the phenomenon was first reported by Auzel (1966).[1] A basic requirement for UC to take place is the availability of more than one metastable excited state. Upconversion is ubiquitous among rare earth (RE) compounds.[2,3,4] Due to their valence electrons in the well-shielded 4f shell, the RE ions often have several metastable f−f excited states. Among the transition metals multiple emitting states are extremely rare, due to the stronger influence of multiphonon relaxation processes. Nevertheless, examples of transition metal (TM) based UC have been reported recently for Ti^{2+},[5] Ni^{2+},[6] Mo^{3+},[7] Re^{4+},[8] and Os^{4+} [9] in various halide lattices.

A new and exciting field is the combination of RE and TM ions, which leads to new pathways for upconversion processes.[10,11] Mixed RE/TM systems provide a very interesting situation, in which d−d excited-state energies of the TM are ligand field dependent, whereas the f−f energies of the RE partner are essentially independent of the ligand field because of shielded f electrons. This allows a selective chemical tuning of TM centered state energies.

Various examples using Yb^{3+} as a sensitizer for UC processes in lanthanide doped crystals and glasses have been demonstrated.[12,13] The Yb^{3+} ion has a [Xe] $4f^{13}$ electron configuration, giving rise to a $^2F_{7/2}$ ground state and only one f−f excited state $^2F_{5/2}$ around 10000 cm^{-1}. UC therefore cannot take place on a single Yb^{3+} ion. This made Yb^{3+} the lanthanide ion of choice for first studies on combined Yb^{3+}/Mn^{2+} systems. We have recently reported efficient near-IR (NIR) to visible (VIS) UC in $RbMnCl_3$:Yb^{3+} and $CsMnCl_3$:Yb^{3+} at cryogenic temperatures.[14,15] The NIR excitation was into the $^2F_{5/2}$ absorption lines of Yb^{3+}, and the red luminescence was assigned to the $^4T_{1g} \rightarrow {}^6A_{1g}$ transition of Mn^{2+}. This observation is surprising and without precedent, and we decided to study the underlying mechanisms in detail. In $RbMnCl_3$:Yb^{3+} we postulate a new type of upconversion mechanism. It is based on exchange interactions between adjacent Yb^{3+} and Mn^{2+} ions in the lattice and enables cooperative electronic transitions involving both ions. In $CsMnCl_3$:Yb^{3+} the UC process is significantly more efficient, and it appears that besides an exchange mechanism there is a strong contribution by an energy transfer (ET) mechanism.[16] The structural differences between $RbMnCl_3$ and $CsMnCl_3$ are small, and it is not understood which are the determinant factors for the mechanisms and the efficiency of the UC process. To get more insight we systematically vary the chemical composition and the crystal structure.

$CsMnBr_3$ crystallizes in the $CsNiCl_3$ structure type with face-sharing $MnBr_6^{4-}$ units forming $MnBr_3$ chains and Cs^+ ions located between the chains (details see Sec 4.1).[17] In contrast to $RbMnCl_3$ and $CsMnCl_3$, in which both face-sharing and corner-sharing connections between the $MnCl_6^{4-}$ units occur, the situation is simplified in the title compound. RE^{3+} dopant ions are known to predominantly enter this structure in well-defined pairs, as illustrated in Figure 1.[18,19] Compared to the chlorides, the bromides provide a smaller ligand field, and therefore the Mn^{2+} $^4T_{1g}$ state is shifted to higher energies.

---

(1) Auzel, M. F. *C. R. Acad. Sci.* **1966**, *262*, 1016.
(2) Cockroft, N. J.; Jones, G. D.; Nguyen, D. C. *Phys. Rev. B* **1992**, *45*, 5187.
(3) Wenger, O. S.; Gamelin, D. R.; Butashin, A. V.; Kaminskii, A. A.; Güdel, H. U. *Phys Rev. B* **1999**, *60*, 5312.
(4) Krämer, K.; Güdel, H. U.; Schwartz, R. N. *J. Alloys Compd.* **1998**, *275−277*, 191.
(5) Jacobsen, S. M.; Güdel, H. U. *J. Lumin.* **1989**, *43*, 125.
(6) Oetliker, U.; Riley, M. J.; May, P. S.; Güdel, H. U. *Coord. Chem. Rev.* **1991**, *111*, 125.
(7) Gamelin, D. R.; Güdel, H. U. *J. Am. Chem. Soc.* **1998**, *120*, 12143.
(8) Gamelin, D. R.; Güdel, H. U. *Inorg. Chem.* **1999**, *38*, 5154.
(9) Wermuth, M.; Güdel, H. U. *J. Am. Chem. Soc.* **1999**, *121*, 10102.
(10) Heer, S.; Wermuth, M., Krämer, K.; Güdel, H. U. *Chem. Phys. Lett.* **2001**, *334*, 293.
(11) Kirk, A. D.; Furer, N.; Güdel, H. U. *J. Lumin.* **1996**, *68*, 77.
(12) Ostermayer, F. W.; van der Ziel, J. P. M.; Marcos, H. M.; van Uitert, L. G.; Geusic, J. E. *Phys. Rev. B* **1971**, *3*, 2698.
(13) Watts, R. K.; Richter, H. J. *Phys. Rev. B* **1970**, *1*, 4208.
(14) Valiente, R.; Wenger, O. S.; Güdel, H. U. *Chem. Phys Lett.* **2000**, *320*, 639.
(15) Valiente, R.; Wenger, O. S.; Güdel, H. U. *Phys. Rev. B* **2001**, *63*, 165102.
(16) Valiente, R.; Wenger, O. S.; Güdel, H. U. To be published.
(17) Goodyear, J.; Kennedy, D. J. *Acta Crystallogr.* **1972**, *B28*, 1640.
(18) McPherson, G. L.; Henling, L. M. *Phys. Rev. B* **1977**, *16*, 1889.
(19) Henling, L. M.; McPherson, G. L. *Phys. Rev. B* **1977**, *16*, 4756.

10.1021/ic010081f CCC: $20.00

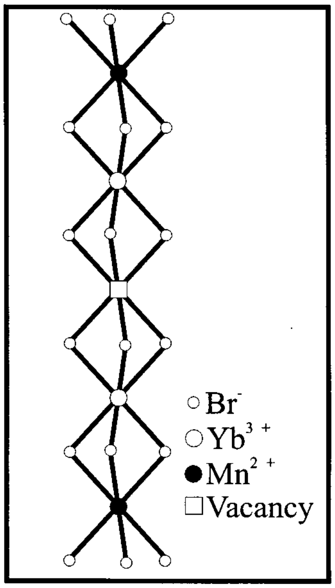

Figure 1. Schematic representation of the linear chain structure of $CsMnBr_3$:0.5%Yb^{3+} with the Yb^{3+} sites.

In addition, nonradiative relaxation processes are less competitive in a bromide than in a chloride due to the smaller vibrational energies. This should enhance the probability of both upconversion and VIS luminescence processes.

2. Experimental Section

2.1. Crystal Growth and Manipulation. Single crystals of Yb^{3+} doped $CsMnBr_3$ were grown by the Bridgman technique from a stoichiometric mixture of CsBr and $MnBr_2$ with addition of 0.5% $YbBr_3$. The real ytterbium concentration of 0.5 ± 0.1 mol % was measured by ICP-OES. Samples with good optical quality were obtained and checked by X-ray powder diffraction. The *c*-axis was optically identified using a polarizing microscope, and crystal pieces were then cut parallel to the *c*-axis. Both the starting materials and the crystals are hygroscopic, therefore all the handling was carried out in a glovebox under N_2 atmosphere. For the experiments crystals were mounted in a sealed copper cell or in closed quartz glass ampules with He atmosphere.

2.2. Spectroscopic Measurements. Sample cooling for absorption measurements was achieved using a closed cycle cryostat (Air Products). The He-flow tube technique was used for emission experiments. Polarized absorption spectra were measured on a Cary 5E (Varian) spectrometer with $E||c$ (π) and $E\perp c$ (σ), where c is the hexagonal axis of the $CsMnBr_3$ crystals. UC was excited with an Ar^+ ion laser (Spectra Physics 2060−10 SA) pumped tunable Ti:sapphire laser (Spectra Physics 3900S). Wavelength control was achieved by an inchworm driven (Burleigh PZ-501) birefringent filter and a wavemeter (Burleigh WA2100). The sample luminescence was dispersed by 0.85 m double monochromator (Spex 1402) with 500 nm blazed 1200 groves/mm gratings. VIS and NIR luminescence were detected by cooled photomultiplier tubes (RCA C31034 and Hamamatsu 3310−01, respectively) in connection with a photon-counting system (Stanford Research SR 400). Mn^{2+} luminescence was excited by the 457.9 nm line of the Ar^+ ion laser and detected as described above. The excitation laser beams were focused on the sample with a $f = 53$ mm focal lens. All spectra are corrected for the wavelength dependence of the sensitivity of the monochromator and the detection system (measured with a calibrated 60 W tungsten lamp (2900 K) as a blackbody radiation source) and for the refractive index of air (vacuum correction). The spectra are presented as number of photons versus wavenumber. For the two-color experiment two Ti:sapphire lasers were used as excitation sources. All excitation scans were corrected for the power dependence of the Ti:sapphire laser source over the tuning range. The laser power was measured with a power meter (Coherent Labmaster-E).

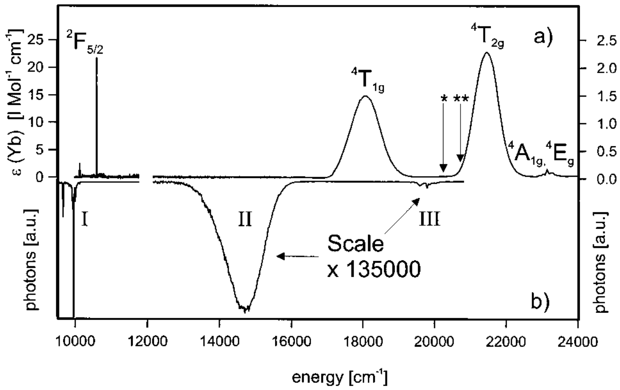

Figure 2. (a) σ-polarized survey absorption spectrum of $CsMnBr_3$: 0.5%Yb^{3+} at 12 K. The NIR spectral region shows the $^2F_{7/2}\rightarrow{}^2F_{5/2}$ transition of Yb^{3+}. Bands in the VIS are assigned to the first four d−d transitions of Mn^{2+} (d^5). The asterisk (*) and double asterisk (**) arrows denote the energy reached by excited-state absorption (ESA) transitions originating from the $^2F_{5/2}$ excited state with 10 138 cm^{-1} and 10 596 cm^{-1} laser energies, respectively. (b) 12 K survey luminescence spectra after NIR excitation into the most intense Yb^{3+} $^2F_{5/2}$ absorption line at 10 596 cm^{-1}. (I) Yb^{3+} $^2F_{5/2}\rightarrow{}^2F_{7/2}$ luminescence, (II) red Mn^{2+} $^4T_{1g}\rightarrow{}^6A_{1g}$ UC luminescence, (III) green cooperative Yb^{3+} pair UC luminescence. The emission bands (II) and (III) are magnified by a factor of 135 000 relative to feature (I).

For time-resolved measurements 10 ns pulses of the second harmonic of a Nd:YAG (Quanta Ray DC R 3) pumped dye laser (Lambda Physik FL3002; Pyridine 1 in methanol) were Raman shifted (Quanta Ray, RS-1, H_2, 340 psi, operative range 935−1025 nm). Square wave pulses in the same spectral range were generated with an acousto-optic modulator (Coherent 305) controlled by a function generator (Stanford Research Systems DS345). For these pulsed experiments the sample luminescence was dispersed by a 0.75 m single monochromator (Spex 1702) equipped with a 750 nm blazed 600 grooves/mm grating and detected with a photomultiplier (Hamamatsu 3310−01) and a multichannel scaler (Standford Research SR430).

3. Results

Figure 2a presents the σ-polarized 12 K absorption spectrum covering the relevant region for upconversion between 10 000 and 24 000 cm^{-1}. The sharp features just above 10 000 cm^{-1} are due to $^2F_{7/2}\rightarrow{}^2F_{5/2}$ transitions of Yb^{3+} and the absorption bands above 17 000 cm^{-1} are assigned to $CsMnBr_3$ excitation from a comparison with published results.[20] Whereas the σ and π polarized spectra are distinctly different in the $CsMnBr_3$ part of the spectrum, these differences are small in the region of Yb^{3+} absorptions. The absorption bands centered at 18100, 21450 and 23150 cm^{-1} in Figure 2a are due to $^4T_{1g}$, $^4T_{2g}$, and $^4A_{1g}$/^4E_g excitations of Mn^{2+}, respectively. Figure 2b shows an unpolarized survey luminescence spectrum (upside down) at 12 K after excitation into the dominant Yb^{3+} $^2F_{5/2}$ absorption line at 10 596 cm^{-1}. Besides the Yb^{3+} luminescence (band I), two different visible UC emission bands are observed. The broad band II centered around 14700 cm^{-1} is ascribed to the $^4T_{1g}\rightarrow{}^6A_{1g}$ emission of Mn^{2+}, and the weak and sharp structured band III around 19 800 cm^{-1} is ascribed to a cooperative Yb^{3+} pair emission. Note the different scales for the VIS and NIR emissions in Figure 2b.

For excitation of the Yb^{3+} $^2F_{5/2}$ level at 10596 cm^{-1} with a typical laser power of 150 mW at 12 K (beam focused with a 53 mm focal lens), the following ratios of emitted photons were derived: band III, 0.0004%; band II, 0.035%; band I, 99.9%.

Figure 3 presents the Mn^{2+} $^4T_{1g}\rightarrow{}^6A_{1g}$ luminescence intensity as a function of temperature for 10596 cm^{-1} (trace a) and 21838

---

(20) McCarthy, P. J.; Güdel, H. U. *Inorg. Chem.* **1984**, *23*, 880.

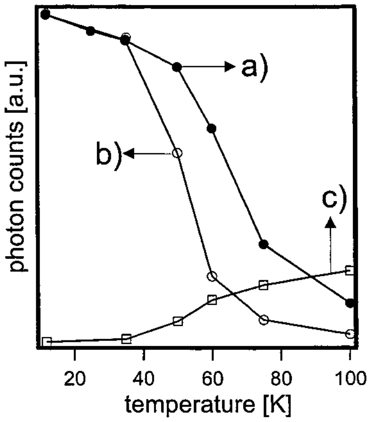

Figure 3. The temperature dependence between 12 and 100 K of Mn^{2+} $^4T_{1g}\rightarrow{}^6A_{1g}$ luminescence intensity (a) after Yb^{3+} excitation at 10 596 cm^{-1} (b) after direct Mn^{2+} excitation at 21 838 cm^{-1}. Trace c shows the intensity of the Yb^{3+} NIR luminescence after Mn^{2+} excitation. Traces b and c are on the same scale; trace a is arbitrarily scaled to same emission as trace b at 12 K.

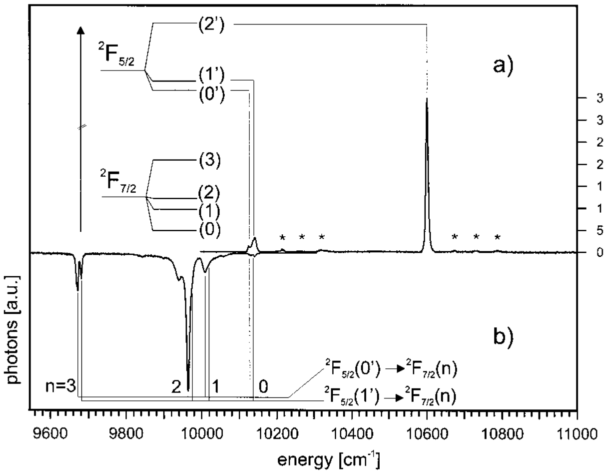

Figure 4. (a) Unpolarized high-resolution absorption spectrum of $CsMnBr_3$: 0.5% Yb^{3+} in the Yb^{3+} $^2F_{7/2}\rightarrow{}^2F_{5/2}$ region at 12 K. Assignments to the crystal field levels of the $^2F_{5/2}$ (0′, 1′, 2′) are given. Asterisks (*) denote vibronic sidebands. (b) 12 K Yb^{3+} $^2F_{5/2}\rightarrow{}^2F_{7/2}$ luminescence after excitation at 10596 cm^{-1}. Assignments to the crystal field levels $^2F_{7/2}$(0, 1, 2, 3) are given. The energies of all the Yb^{3+} crystal field levels are summarized in Tab. 1.

cm^{-1} excitation (trace b), respectively. The 12 K points were arbitrarily scaled to the same value in order to bring out the temperature dependence. The green excitation at 21838 cm^{-1} also induces NIR luminescence. Trace c shows the evolution of Yb^{3+} $^2F_{5/2}\rightarrow{}^2F_{7/2}$ luminescence intensity as a function of temperature. The data in traces b and c are corrected for the varying absorption cross-section at the laser wavelength.

Figure 4 shows the high-resolution unpolarized absorption (a) and luminescence (b, upside down) spectra in the $^2F_{5/2}\leftrightarrow{}^2F_{7/2}$ transition region of Yb^{3+}. The band energies are presented and discussed in section 4.2, and in Table 1 the crystal-field level energies are summarized.

In Figure 5 the green emission band III of Figure 2b is enlarged. It was obtained by excitation into the intense 10596 cm^{-1} absorption line of Yb^{3+} at 12 K.

Figure 6 presents the time evolution of (a) the green Yb^{3+} pair UC luminescence monitored at 19 802 cm^{-1} and (b) the NIR Yb^{3+} $^2F_{5/2}\rightarrow{}^2F_{7/2}$ luminescence monitored at 9964 cm^{-1} at 12 K, after excitation at 10596 cm^{-1} with square wave pulses of 5 ms width, in a semilogarithmic representation. Single-exponential fits to the experimental data are shown as straight lines. From these fits lifetimes of 344 μs (a) and 704 μs (b) were extracted. The lifetimes were found to essentially remain constant between 12 and 100 K.

Table 1. Crystal-Field Level Energies of the Yb^{3+} Multiplets in $CsMnBr_3$:0.5%Yb^3 [a]

free ion term	crystal-field level	energy [cm^{-1}]
$^2F_{5/2}$	(2′)	10596
	(1′)	10138
	(0′)	10126
$^2F_{7/2}$	(3)	454
	(2)	162
	(1)	118
	(0)	0

[a] All the energies are given relative to the ground level $^2F_{7/2}(0)$.

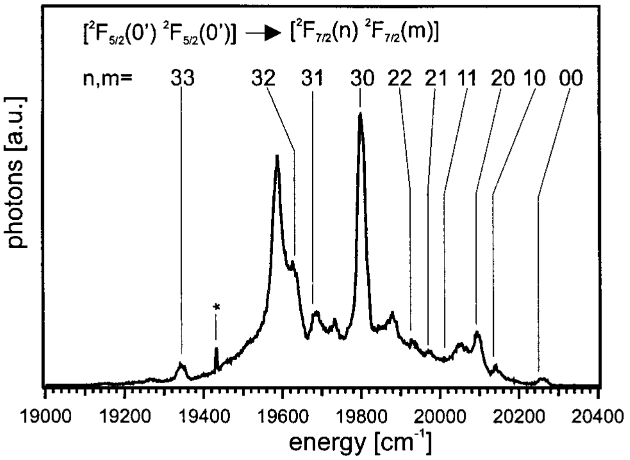

Figure 5. 12 K cooperative $[^2F_{5/2}(0')-{}^2F_{5/2}(0')]\rightarrow[^2F_{7/2}(n)-{}^2F_{7/2}(m)]$ Yb^{3+} pair UC luminescence spectrum after NIR excitation at 10596 cm^{-1}. Individual peaks are assigned based on a calculation from Yb^{3+} $^2F_{5/2}\rightarrow{}^2F_{7/2}$ emission energies (Figure 4 and Table 1). The asterisk (*) indicates a peak due to stray light of the Ar^+-laser (514.5 nm line).

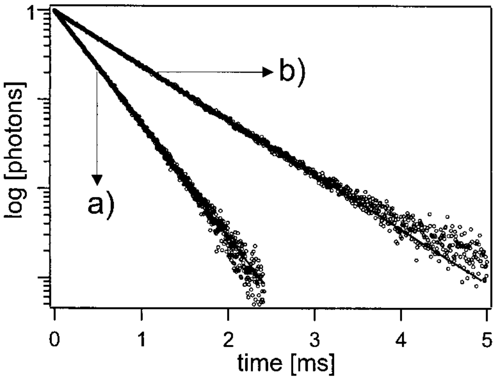

Figure 6. Time evolution of the luminescence intensity at 12 K after 5 ms square wave pulse excitation at 10596 cm^{-1} in semilogarithmic representation. (a) Monitoring green cooperative Yb^{3+} pair luminescence at 19 800 cm^{-1}. (b) Monitoring NIR Yb^{3+} $^2F_{5/2}(0')\rightarrow{}^2F_{7/2}(2)$ emission at 9964 cm^{-1}. The straight lines denote single-exponential fits to the experimental data.

In Figure 7 trace a shows Mn^{2+} $^4T_{1g}\rightarrow{}^6A_{1g}$ UC luminescence observed after Yb^{3+} excitation at 10596 cm^{-1} at 12 K with a typical laser power of 150 mW. For direct comparison trace b shows the 12 K Mn^{2+} $^4T_{1g}\rightarrow{}^6A_{1g}$ luminescence obtained after direct Mn^{2+} excitation at 21 838 cm^{-1}. Identical band shapes are observed but the UC luminescence band maximum is red-shifted by 130 cm^{-1}. The inset of Figure 7 shows a double logarithmic representation of the UC luminescence intensity as

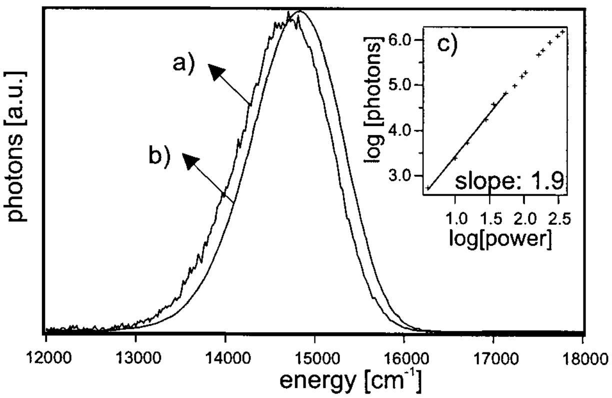

Figure 7. (a) 12 K Mn^{2+} $^4T_{1g}\rightarrow{}^6A_{1g}$ UC emission after Yb^{3+} excitation at 10596 cm^{-1}. (b) 12 K Mn^{2+} $^4T_{1g}\rightarrow{}^6A_{1g}$ emission after direct Mn^{2+} $^4T_{2g}$ excitation at 21 838 cm^{-1}. (c) Mn^{2+} $^4T_{1g}\rightarrow{}^6A_{1g}$ UC photon counts versus 10 596 cm^{-1} excitation laser power at 12 K in double logarithmic representation.

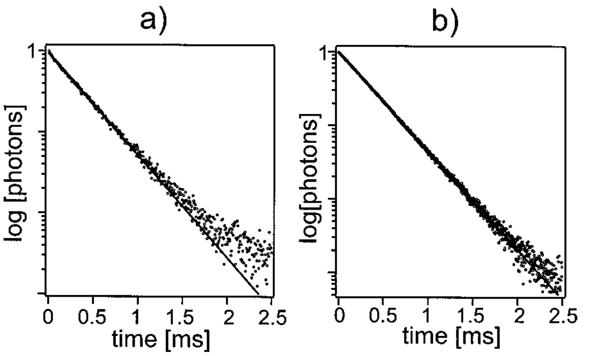

Figure 8. Time evolution of the Mn^{2+} $^4T_{1g}\rightarrow{}^6A_{1g}$ luminescence intensity at 12 K after excitation in semilogarithmic representation: (a) 10 ns pulses at 10 596 cm^{-1} (upconversion) and (b) 5 ms square wave pulses at 21 388 cm^{-1} (direct excitation). The straight lines represent single-exponential fits to the experimental data.

a function of the laser power at 12 K after excitation at 10 596 cm^{-1}. A linear fit to the data up to a laser power of 50 mW yields a slope of 1.9. At higher powers the slope decreases. This is the typical behavior of a two-photon process.[21]

Figure 8a shows the temporal evolution of the 12 K Mn^{2+} $^4T_{1g}\rightarrow{}^6A_{1g}$ luminescence at 14 700 cm^{-1} after excitation with 10 ns short pulses at 10 596 cm^{-1} (UC excitation). Figure 8b shows the decay of the Mn^{2+} luminescence at 12 K after direct Mn^{2+} excitation with square wave pulses of 5 ms width at 21 838 cm^{-1}. We note that both decay curves are very similar. They can be fitted with single-exponential decay functions with the following decay times: $\tau = 337$ μs (a) and $\tau = 324$ μs (b) (see full lines in Figure 8). The time evolution of the UC luminescence was also measured for excitation into the weak 10138 cm^{-1} absorption line of Yb^{3+} (see Figure 4) with a very similar result as in (a) and a decay time of $\tau = 332$ μs. The important result of these measurements is the absence of a rise in the UC data of (a), as will be discussed in section 4.4.5.

The temporal behavior of Mn^{2+} $^4T_{1g}\rightarrow{}^6A_{1g}$ luminescence was studied as a function of temperature between 12 and 100 K after excitation with square wave pulses of 5 ms width at 21 838 cm^{-1} (data not shown). The decay curves were found to be reproduced by single-exponential fits up to 35 K and at higher temperatures became more and more nonsingle-exponential character with a fast and a slow decay component. The lifetime of the faster component was found to decrease in parallel with the emission intensity (see Figure 3b) from 324 μs at 12 K to ~1μs at 100 K.

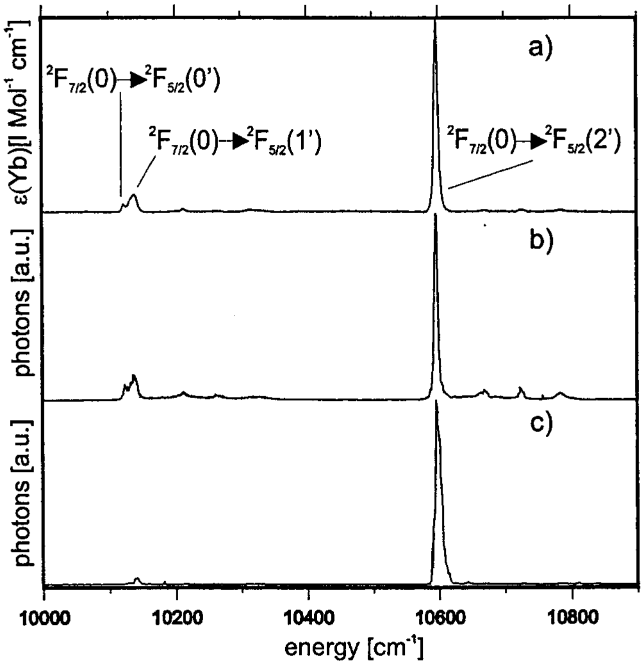

Figure 9. (a) 12 K absorption spectrum in the Yb^{3+} $^2F_{7/2}\rightarrow{}^2F_{5/2}$ transition region. (b) 12 K excitation spectrum monitoring 9960 cm^{-1} Yb^{3+} $^2F_{5/2}(0')\rightarrow{}^2F_{7/2}(2)$ emission. (c) 12 K excitation spectrum monitoring Mn^{2+} $^4T_{1g}\rightarrow{}^6A_{1g}$ UC emission at 14 814 cm^{-1}.

Figure 9 presents the unpolarized 12 K absorption spectrum of Yb^{3+} in the NIR in trace a, the corresponding 12 K excitation spectrum of the most intense NIR Yb^{3+} luminescence peak at 9960 cm^{-1} in trace b and in trace c the 12 K upconversion excitation spectrum of the Mn^{2+} $^4T_{1g}\rightarrow{}^6A_{1g}$ luminescence at 14814 cm^{-1}. The upconversion excitation spectrum of the green cooperative Yb^{3+} pair luminescence at 19 800 cm^{-1} is not shown; it is similar to trace c. We note that the spectra a and b are very similar, as expected for the linear excitation process in the experiment (b). The band positions in spectrum c are the same as in (a) and (b), but the relative intensities are significantly different. This is a direct reflection of the nonlinear nature of the UC excitation process in (c), as will be discussed in section 4.4.5. Taking the intensity ratio of the weak double band around 10 130 cm^{-1} and the strong band at 10 596 cm^{-1} as an indicator we find the following values: 1/8 in (b), 1/38 in (c), and 1/56 for the green Yb^{3+} UC luminescence (not shown).

Figure 10 shows on the left-hand side the result of excited-state excitation (ESE) experiments, which are described and discussed in detail in Sec. 4.4.5.

4. Discussion

4.1. Crystal Structure of the CsMnBr$_3$ Host Lattice and the Yb^{3+} Dopant Site.

CsMnBr$_3$ crystallizes in the space group $P6_3/mmc$ with unit cell parameters $a = 7.609(15)$ Å and $c =$ 6,52(5) Å.[17] It is isomorphous with CsNiCl$_3$. The linear chains of face-sharing MnBr$_6^{4-}$ octahedra (see Figure 1) run parallel to the c-axis. Individual chains are separated by Cs$^+$ ions. The MnBr$_6^{4-}$ octahedra are slightly trigonally distorted to D_{3d} site symmetry. The interchain Mn^{2+}−Mn^{2+} distance is 7.61 Å, more than twice the intrachain Mn^{2+}−Mn^{2+} spacing of 3.26 Å. This leads to a pronounced anisotropy in the magnetic behavior: A transition to 3-D magnetic order occurs at 8.3 K, but antiferromagnetic 1-D correlations persist to much higher temperatures.

---

[21] Pollnau, M.; Gamelin, D. R.; Lüthi, S. R.; Hehlen, M. P.; Güdel, H. U. *Phys. Rev. B* **2000**, *61*, 3337.

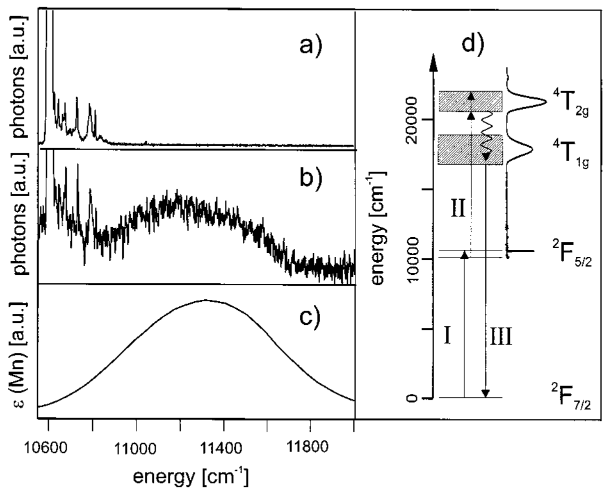

Figure 10. (d) Relevant energy level scheme for two-laser experiment. (I) Laser beam fixed at 10 596 cm^{-1} with a power of 7 mW. (II) Tunable laser beam with a power of more than 100 mW over the whole tuning range. (III) Monitored Mn^{2+} $^4T_{1g} \rightarrow {}^6A_{1g}$ UC luminescence at 14814 cm^{-1}. (a) Experimental result at 12 K without laser I. (b) 12 K ESE experiment with laser I fixed and laser II tuned. The *y*-axis of (a) and (b) are chosen to have equal intensity of the Yb^{3+} (0)→(2′) line. (c) The Mn^{2+} $^4T_{2g}$ absorption band at 12 K downshifted in energy by 10 126 cm^{-1}.

The following anti-ferromagnetic exchange parameters have been derived: $J_{\rm intrachain} = -7.1$ cm^{-1}, $J_{\rm interchain} = -0.015$ cm^{-1}.[22,23]

Yb^{3+} ions are most likely to substitute for Mn^{2+} ions when doped into CsMnBr$_3$. For charge compensation a special arrangement of the Yb^{3+} dopant ions is predominant. It has been established by EPR spectroscopy for the isostructural CsCdBr$_3$ that more than 90% of the Gd^{3+} dopant ions enter the chain structure in a Gd^{3+}−vacancy−Gd^{3+} arrangement, where the vacancy at the Cd^{2+} site ensures charge compensation.[18,19] The local site symmetry for the RE^{3+} ions in this arrangement is C_{3v}. For various RE^{3+} ions in CsCdBr$_3$ asymmetric pairs (RE^{3+}−RE^{3+}−vacancy) were identified as minority centers. Our spectra clearly show a predominance of one Yb^{3+} site, and further evidence discussed below make it very plausible that it is the Yb^{3+}−vacancy−Yb^{3+} site shown in Figure 1.

4.2. Yb^{3+} Spectroscopy: Energy Levels and Emission Properties. Absorption and luminescence transitions of Yb^{3+} are observed as sharp features around 10 000 cm^{-1}. Yb^{3+} has a 4f^{13} electron configuration leading to a $^2F_{7/2}$ ground term and a $^2F_{5/2}$ as the only excited term. The absence of any other but the $^2F_{5/2}$ excited term makes Yb^{3+} an attractive ingredient in numerous optical materials. This is also true in the present situation. The upconversion phenomenon reported here largely depends on the absence of any excited Yb^{3+} levels in the VIS. The first allowed excitation in YbBr$_6^{3-}$ is a ligand-to-metal charge-transfer transition with an absorption band above 25 000 cm^{-1}, i.e., outside of the relevant energy range of this study.

In the C_{3v} site symmetry the Yb^{3+} $^2F_{7/2}$ ground term and the Yb^{3+} $^2F_{5/2}$ excited term are split into four (0, 1, 2, 3) and three (0′, 1′, 2′) crystal-field levels, respectively. Absorption transitions from the energetically lowest component of the $^2F_{7/2}(0)$ to the levels $^2F_{5/2}(0′,1′,2′)$ are found at 10126, 10138, and 10596 cm^{-1}, see spectrum and assignment in Figure 4a. Weak vibronic features on the high-energy side of the electronic transitions are marked with asterisks (*). The Yb^{3+} luminescence spectrum at 12 K in Figure 4b shows the $^2F_{5/2}(0′) \rightarrow {}^2F_{7/2}(0, 1, 2, 3)$ luminescence transitions, which are observed at 10 126, 10 008, 9964, and 9672 cm^{-1}. From these data the crystal-field level energies of the Yb^{3+} $^2F_{7/2}$ and $^2F_{5/2}$ terms were extracted and are summarized in Table 1. In addition a second series of transitions, which are assigned to the $^2F_{5/2}(1′) \rightarrow {}^2F_{7/2}(0, 1, 2, 3)$ transitions, is found shifted to higher energies by 10−12 cm^{-1} at 10 138, 10 018, 9975, and 9682 cm^{-1}. Temperature-dependent emission spectra reveal their hot band character. Due to the small splitting the $^2F_{5/2}(1′)$ level has at 12 K a Boltzmann population of around 25% relative to the $^2F_{5/2}(0′)$ level. Therefore $^2F_{5/2}(1′) \rightarrow {}^2F_{7/2}$ (0, 1, 2, 3) transitions are already observed in the 12 K luminescence spectrum.

In purely octahedral symmetry the levels $^2F_{7/2}(1, 2)$ and $^2F_{5/2}(0′, 1′)$ would be degenerate. From the data in Figure 4 and Table 1 we see that they are split by 44 and 12 cm^{-1}, respectively, which is about an order of magnitude smaller than the total crystal-field splitting of $^2F_{7/2}$ or $^2F_{5/2}$. The trigonal crystal-field component at the Yb^{3+} site is thus relatively small. This does not mean, however, that the Yb^{3+} coordination is close to octahedral. The odd-parity crystal-field component must be very large, because of the weakness of the vibronic sidebands compared to the electronic origins in the Yb^{3+} absorption and emission spectra of Figure 4. Comparison with the corresponding spectra of CsCdBr$_3$:Yb^{3+} shows a nearly perfect match, both in band positions and relative intensities.[24] This is strong support for similar Yb^{3+} sites and charge compensation in the two systems.

The Yb^{3+} $^2F_{5/2} \rightarrow {}^2F_{7/2}$ relaxation is expected to be purely radiative because of the large energy gap of around 10 000 cm^{-1}. CsMnBr$_3$ has a phonon cut off frequency below 200 cm^{-1}, and therefore more than 50 phonons are needed to bridge this energy gap. Assuming a pure electric dipole mechanism for the Yb^{3+} $^2F_{5/2} \rightarrow {}^2F_{7/2}$ transition, the radiative lifetime $\tau_{\rm rad}$ is connected with the oscillator strength by

$$\tau_{\rm rad} = \alpha \frac{\lambda_{\rm ba}^2}{n((n^2+2)/3)^2} \frac{g_{\rm a}}{g_{\rm b}} \frac{1}{f} \qquad (1)$$

where α is a constant (1.5 × 10^4 s m^{-2}), $\lambda_{\rm ba} = 1.004 \times 10^{-6}$ m is the average emission wavelength, $g_{\rm b} = 3$ and $g_{\rm a} = 4$ are

---

(22) Eibschütz, M.; Sherwood, R. C.; Hsu, F. S. L.; Cox, D. E. *AIP Conf. Proc.* **1972**, *10*, 684.

(23) Breitling, W.; Lehman, W.; Weber, R.; Lehner, N.; Wagner, V. *J. Magn. Magn. Mater.* **1977**, *6*, 113.

(24) Goldener, Ph.; Pellé, P.; Meichenin, D.; Auzel, F. E. *J. Lumin.* **1997**, *71*, 137.

(25) Kuznetsova, I. Ya.; Kovaleva, I. S.; Ferdovov, V. A. *Russ. J. Inorg. Chem. (Engl. Transl.)* **1989**, *34*, 568, RJICAQ.

(26) Solomon, E. I.; McClure, D. S. *Phys. Rev. B* **1974**, *9*, 4690.

(27) Kambli, U. Ph.D. thesis, Bern, 1984.

(28) McPherson, G. L.; Auerbach, R. A.; Kwawer, N.; Talluto, K. F. *J. Lumin.* **1984**, *31 & 32*, 296.

(29) McPherson, G. L.; Talluto, K.; Auerbach, R. A. *Solid State Commun.* **1982**, *43*, 817.

(30) Knochenmuss, R.; Güdel, H. U. *J. Chem. Phys.* **1987**, *86*, 1104.

(31) Nakazawa, E.; Shionaya, S. *Phys. Rev. Lett.* **1970**, *25*, 1710.

(32) Hehlen, M. P.; Güdel, H. U. *J. Chem. Phys.* **1993**, *98*, 1768.

(33) Oomen, EWJL *Adv. Mater.* **1991**, *3*, 403.

(34) Ovsyankin, V. V.; Feofilov, P. *JEPT Lett.* **1966**, *3*, 317.

(35) Güdel, H. U. *Comments Inorg. Chem.* **1984**, *3* 189.

(36) Güdel, H. U.; Dubicki, L. *Chem. Phys.* **1974**, *6*, 272.

(37) Ovsyankin, V. V. *Modern Problems in Condensed Matter Sciences*; North-Holland: Amsterdam **1987**, 343.

(38) van der Ziel, J. P.; van Uitert, L. G. *Phys. Rev.* **1969**, *180*, 343.

(39) van der Ziel, J. P.; van Uitert, L. G. *Phys. Rev. B* **1973**, *8*, 1889.

(40) Ferguson, J.; Guggenheim, H. J.; Tanabe, Y. *J. Phys. Soc. Jpn.* **1966**, *21*, 692.

(41) Jacobsen, S. M.; Güdel, H. U.; Smith, W. E. *Inorg. Chem.* **1987**, *26*, 2001.

(42) Reinhard, C.; Valiente, R.; Güdel, H. U. To be published.

the degeneracies of the involved states $^2F_{5/2}$ and $^2F_{7/2}$, and $n = 1.78$ is the refractive index averaged over all polarizations (from data for $CsCdBr_3$[25]). From the absorption spectrum in Figure 2a, we extracted an oscillator strength $f = 2.69 \times 10^{-6}$. The calculated lifetime of 798 μs using eq 1 is 13% longer than the measured lifetime of 704 μs at 12 K. Considering the fact that we are using f and τ values measured at low temperature this good agreement confirms the absence of multiphonon relaxation from $^2F_{5/2}$ below 100 K.

4.3. Mn^{2+} Excitations and Dynamics. Mn^{2+} has the [Ar]d^5 electron configuration with a $^6A_{1g}$ ground state for high-spin compounds such as $CsMnBr_3$. All the d−d excitations are both spin and parity forbidden and thus very weak. In $CsMnBr_3$ the observed ϵ-values (see Figure 2a) are enhanced by about an order of magnitude due to exchange interactions.

The lowest energy absorption bands centered at 18 100 and 21 450 cm^{-1} in Figure 2a correspond to $^6A_{1g} \rightarrow {}^4T_{1g}$ and $^4T_{2g}$ excitations, respectively. Both transitions induce an $e_g \rightarrow t_{2g}$ electron promotion and are thus accompanied by changes in the equilibrium geometry. These have been studied in detail in $RbMnF_3$ and found to have contributions along both the totally symmetric a_{1g} and the Jahn−Teller e_g normal coordinates.[26] The observed Stokes shift of 3300 cm^{-1} between the $^6A_{1g} \leftrightarrow {}^4T_{1g}$ absorption and emission maxima in Figure 2 reflects this distortion in the emitting $^4T_{1g}$ state.

The fast decrease of $^4T_{1g} \rightarrow {}^6A_{1g}$ emission intensity, after direct Mn^{2+} $^4T_{2g}$ excitation (see Figure 3) for temperatures above 35 K, is due to thermally activated 1D-energy migration along the Mn^{2+} chains of $CsMnBr_3$, followed by energy transfer to traps.[27] Two types of traps are relevant in $CsMnBr_3$:0.5%Yb^{3+}. One type are killer traps such as Cu^{2+}, Fe^{2+}, or Mn^{3+}, which are always present as impurities in ppm concentration in such crystals.[28,29] The other relevant traps are Yb^{3+} ions, and this process will be discussed in section 4.4.7.

The decay of the $^4T_{1g}$ emission in the title compound is close to single exponential at 12 K, see Figure 8. The lifetimes derived from the 12 K data are $\tau = 324$ μs for direct Mn^{2+} excitation (Figure 8b) and $\tau = 337$ μs for UC excitation via Yb^{3+} (Figure 8a). Both are reasonably close to the literature lifetime of $\tau = 340$ μs of pure $CsMnBr_3$ at this temperature.[27] Above 35 K the decay curves become increasingly nonsingle exponential, irrespective of the mode of excitation. This can have two reasons. In $CsMnBr_3$ the energy migration is expected to be extremely anisotropic with a much higher rate along the chains. As has been shown in detail for TMMC, another 1-D Mn^{2+} crystal, this leads to significant deviations from single-exponential decay behavior.[30] Alternatively, the deviations from exponential decay behavior may be due to a superposition of emissions from Mn^{2+} ions in slightly different sites.

4.4. Upconversion. 4.4.1. General Remarks. The very weak green emission around 19 800 cm^{-1} is due to a cooperative upconversion process in Yb^{3+} pairs, and the more prominent UC band centered around 14 700 cm^{-1} is ascribed to $^4T_{1g} \rightarrow {}^6A_{1g}$ luminescence of Mn^{2+}. This is a remarkable observation in itself, and with the exception of our very recent brief report on Yb^{3+} doped $RbMnCl_3$ and $CsMnCl_3$,[14,15] it is without precedent. The involvement of Mn^{2+} in an upconversion process is unexpected and not understood. The same is not true for the green Yb^{3+} pair emission, which has been observed in numerous Yb^{3+} compounds.[24,31,32] The remarkable feature of the title compound is the presence of both green and red UC emissions, which will turn out to be valuable in the analysis. In Yb^{3+} doped $RbMnCl_3$ and $CsMnCl_3$ the cooperative Yb^{3+} pair emission around 19 800 cm^{-1} was not observed due to Mn^{2+} absorption in this spectral region. In the title compound it happens to lie exactly in the window between the $^4T_{1g}$ and $^4T_{2g}$ absorption bands at 12 K, see Figure 2. In the following sections we will discuss possible mechanisms for the observed upconversion processes.

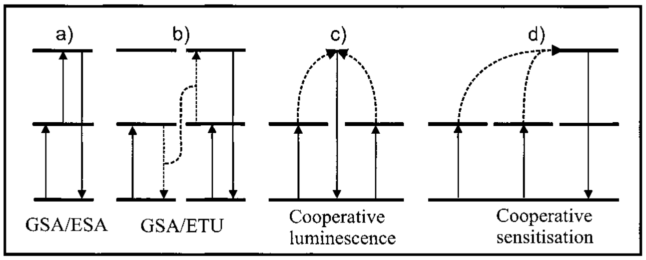

Figure 11. Schematic representation of relevant photon upconversion mechanisms (described in section 4.4.2). The abbreviations GSA and ESA denote ground-state absorption and excited-state absorption processes, respectively. Full arrows correspond to radiative processes and dashed arrows represent nonradiative processes.

4.4.2. Upconversion Mechanisms. Figure 11 schematically summarizes the most important upconversion mechanisms, relevant for our situation in a simple 3-level picture.

Figure 11a shows that the GSA/ESA mechanism is based on two consecutive absorption steps: by ground state absorption (GSA) to a metastable intermediate state and by excited state absorption (ESA) of a second photon the final state is reached. This process usually occurs on a single ion. In experiments with short excitation pulses a pure decay of the UC luminescence is observed after the pulse because both GSA and ESA steps must take place during the laser pulse. This mechanism is widespread and very well characterized in RE^{3+} doped crystals and glasses.[4,33]

Figure 11b shows GSA/ETU or energy transfer upconversion.[1] Two ions in close proximity are excited by GSA to their respective metastable intermediate states. This is followed by a nonradiative energy transfer process leading to one ion in the final state and the second one in the ground state. In pulsed experiments a rise of the UC luminescence intensity following the pulse and preceding the decay is observed. The pulse deposits the excitation in the intermediate state, and the UC proceeds from there. This mechanism is well established in lanthanide systems.

Figure 11c shows cooperative luminescence: In this case the ions involved do not have a stationary state at the emitting level. Two ions in close proximity are both excited to the same excited state and then they combine these excitations in a cooperative process to emit a photon at twice the excitation energy. The UC luminescence decays immediately after an excitation pulse in this mechanism. The green emission of many Yb^{3+} compounds has been ascribed to this mechanism.[24,31,32]

Figure 11d shows cooperative sensitization: Two excited donor ions simultaneously transfer their excitation energy to an acceptor ion, which has an excited state at twice the excitation energy.[34] This is a three-ion process, which requires the three ions to be in close proximity. It has been postulated to account for upconversion phenomena in BaF_2 and YF_3 codoped with Yb^{3+} and Tb^{3+}. This mechanism is not well characterized, but it is a potential candidate for the UC behavior of the title compound. As a consequence of the nonradiative energy transfer step, we expect the UC luminescence transient after an excitation pulse to exhibit a rise followed by the decay.

4.4.3. Green Cooperative Yb^{3+} Pair UC Luminescence. The structured green UC luminescence band III in Figure 2b, which is enlarged in Figure 5, is readily assigned to a cooperative upconversion process according to mechanism c

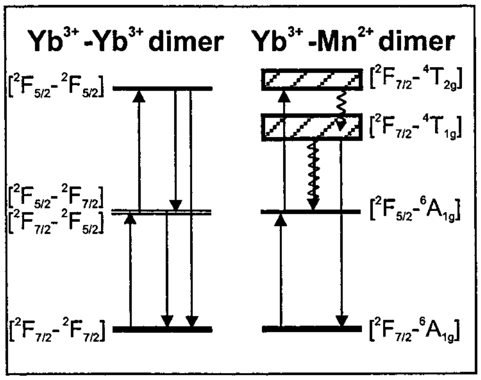

Figure 12. Schematic representation of the relevant upconversion and relaxation mechanisms in $CsMnBr_3:Yb^{3+}$ using dimer notation. The processes are discussed in detail in sections 4.4.3 (Yb^{3+} dimer) and 4.4.6 ($Yb^{3+}-Mn^{2+}$ dimer). Straight and curly arrows represent radiative and nonradiative processes, respectively.

in Figure 11. Its occurrence has been reported for Yb^{3+} in various ligand environments.[10,31,32] The energy and fine structure of the band in $CsMnBr_3$:0.5%Yb^{3+} is strikingly similar to that reported in $CsCdBr_3:Yb^{3+}$.[24] Also the ratio of photons emitted in the NIR to photons emitted in the green is in the same order of magnitude in both compounds. These similarities are ascribed to the similar crystal structures of $CsMnBr_3$ and $CsCdBr_3$ and the resulting similar Yb^{3+}−vacancy−Yb^{3+} sites shown in Figure 1. This dimerization of the Yb^{3+} ions in the chain structure favors cooperative behavior. We choose a dimer for our discussion. The ground, intermediate and emitting state are then designated as $[^2F_{7/2}-^2F_{7/2}]$, $[^2F_{7/2}-^2F_{5/2}]/[^2F_{5/2}-^2F_{7/2}]$, and $[^2F_{5/2}-^2F_{5/2}]$, respectively. This is shown on the left of Figure 12. In contrast to the picture in Figure 11c the emitting state is a real stationary state in this dimer picture. It is a doubly excited dimer state; quite analogous to the well characterized doubly excited exchange-coupled Cr^{3+} dimers.[35] Since the coupling of the two Yb^{3+} excitations, either by exchange or multipole−multipole interactions, is very small in our system,[24] luminescence transition energies should be predictable by addition of observed Yb^{3+} single ion $^2F_{5/2}(0', 1') \rightarrow {}^2F_{7/2}(0, 1, 2, 3)$ transition energies (see Figure 4). The assignments shown in Figure 5 are the result of this calculation. The calculated and the experimental peak energies agree very well, but their relative intensities cannot be correlated with those in the NIR emission spectrum of Figure 4. A number of bands in Figure 5, including a prominent one at 19 587 cm^{-1}, cannot be accounted for by this analysis. We ascribe them to a cooperative vibronic mechanism.[36] As reported in section 3 there are different intensity ratios of the $^2F_{7/2}(0) \rightarrow {}^2F_{5/2}(1')$ to $^2F_{7/2}(0) \rightarrow {}^2F_{5/2}(2')$ lines in the 12 K excitation spectrum when monitoring the NIR and the green Yb^{3+} emissions: 1/8 versus 1/56, respectively. This is a reflection of the nonlinear character of the upconversion excitation. In first-order we expect the excitation spectrum of the UC emission to be the square of the NIR emission. The above ratios confirm this very nicely.

A final point concerns the lifetimes of $\tau = 704$ μs and $\tau = 344$ μs at 12 K of the NIR and green Yb^{3+} luminescence, see the data in Figure 6. Theoretically we expect a ratio of 2/1 due to the 2-fold degeneracy $[^2F_{7/2}-^2F_{5/2}]/[^2F_{5/2}-^2F_{7/2}]$ of the intermediate state, see Figure 12.[37] It is important to note that the lifetime $\tau = 344$ μs is not determined by the green emission process, but by the emission of NIR photons according to $[^2F_{5/2}-^2F_{5/2}] \rightarrow [^2F_{7/2}-^2F_{5/2}]/[^2F_{5/2}-^2F_{7/2}]$, see Figure 12. The oscillator strength of the cooperative $[^2F_{5/2}-^2F_{5/2}] \rightarrow [^2F_{7/2}-^2F_{7/2}]$ transition is extremely small. In first order it is the square of the excitation process $[^2F_{5/2}-^2F_{5/2}] \rightarrow [^2F_{5/2}-^2F_{7/2}]$. The latter has an oscillator strength of roughly 10^{-6} at 12 K in the title compound, see section 4.2. The double excitation process thus has an oscillator strength of the order of 10^{-12}. Accordingly it is impossible to observe these transitions in the absorption spectrum of $CsMnBr_3$: 0.5%Yb^{3+}.

4.4.4. Red Upconversion Luminescence: Mn^{2+} $^4T_{1g} \rightarrow {}^6A_{1g}$. From the comparison of the red UC luminescence after excitation of Yb^{3+} $^2F_{5/2}$ with the Mn^{2+} $^4T_{1g} \rightarrow {}^6A_{1g}$ luminescence after direct Mn^{2+} $^4T_{2g}$ excitation (see Figure 7) we ascribe the UC luminescence to the Mn^{2+} $^4T_{1g} \rightarrow {}^6A_{1g}$ transition. The significant redshift of 130 cm^{-1} relative to the directly excited Mn^{2+} luminescence is indicative of different Mn^{2+} subsets, which are involved in the upconversion and downconversion processes. Direct excitation of Mn^{2+} into the broad $^4T_{2g}$ absorption band leads to the excitation of all Mn^{2+} ions in the crystal, regardless of their chemical surrounding. The situation is completely different for Mn^{2+} UC luminescence after NIR excitation of Yb^{3+}. At low temperatures UC excitation and emission preferentially occurs on the Mn^{2+} ions in the neighborhood of the Yb^{3+} ions. The Mn^{2+} ions of this UC relevant subset are perturbed by the presence of neighboring Yb^{3+} ions and are exposed to a different crystal field. A slightly larger ionic radius of Yb^{3+} ($r = 0.87$ Å) compared to Mn^{2+} ($r = 0.83$ Å) causes a squeezing of the Mn^{2+} coordination close to the Yb^{3+} ions. As a consequence the crystal-field is slightly increased leading to the observed redshift of the $^4T_{1g}$ emission band. A similar redshift of the Mn^{2+} UC emission has been also reported for $RbMnCl_3:Yb^{3+}$.[15] We now proceed to a detailed characterization of this Yb^{3+} to Mn^{2+} UC process.

4.4.5. Time and Wavelength Dependence of the Mn^{2+} $^4T_{1g} \rightarrow {}^6A_{1g}$ Upconversion Luminescence. A point of major interest is to understand the underlying mechanism of the observed Mn^{2+} $^4T_{1g} \rightarrow {}^6A_{1g}$ UC after NIR Yb^{3+} excitation. The observation of cooperative Yb^{3+} pair luminescence in the green spectral region leads to the question whether the Mn^{2+} UC luminescence is a result of subsequent energy transfer to Mn^{2+} from doubly excited Yb^{3+} pairs according to mechanism d in Figure 11. The temporal evolution of the Mn^{2+} UC luminescence after excitation pulse is the key to answer this question.

From the data in Figure 8a we can immediately rule out such a mechanism because the transient shows no rise between 640 ns and 2.5 μs after the pulse. A rise would be expected for the cooperative sensitization mechanism in Figure 11d, however, because it involves an energy transfer step from the doubly excited Yb^{3+} pair to the Mn^{2+}. If there was an undetectably fast (<640 ns) ET process from doubly excited Yb^{3+} pairs to Mn^{2+}, the lifetime of the green Yb^{3+} pair emission would be reduced accordingly. This is not the case, as shown in Figure 6 and discussed in section 4.4.3. Among the mechanisms in Figure 11b and d are ruled out because they would both involve ET steps. Mechanism c is physically unreasonable. The temporal behavior after an excitation pulse points to GSA/ESA mechanism (Figure 11a). However, this usually takes place on a single ion, and we have clear evidence that both Yb^{3+} and Mn^{2+} ions are involved. We thus have to relax the conditions for the GSA/ESA sequence in our system. The two steps are no longer localized excitations on a given ion. Whereas the first step is still essentially a GSA on the Yb^{3+} ion, the ESA step involves both a Yb^{3+} and a Mn^{2+} ion. The initial state of the ESA process is formally localized on Yb^{3+} and the final state on Mn^{2+}. In 4.4.6 we will introduce a dimer model, which takes account of this rather unusual situation. However, first we discuss two experimental results, which help to clarify the situation. In the excitation spectrum of an upconversion luminescence arising by a GSA/ESA sequence one finds the fingerprint of both excitation steps, or in other words, the excitation spectrum corresponds to the product of the GSA and ESA spectra.[21] We clearly recognize the GSA fingerprint in the UC excitation spectrum in Figure 9c. This GSA fingerprint is given by Figure 9b, and we notice that the ratio of the $^2F_{7/2}(0) \rightarrow {}^2F_{5/2}(1')$ to $^2F_{7/2}(0) \rightarrow {}^2F_{5/2}(2')$ bands in the trace 9c is 1/38, as compared to 1/8 in trace 9b. This difference is a reflection of the ESA step in the UC process. The ESA is about five times more efficient at 10 596 cm^{-1} than at 10 138 cm^{-1}. This can be understood with reference to Figure 2a, where the asterisk (*) and the double asterisk (**) mark the position at which the ESA transition hits the $^4T_{2g}$ band of Mn^{2+} for 10 138 cm^{-1} excitation and 10 596 cm^{-1} excitation, respectively. The $^4T_{2g}$ absorption is steeply rising in this region, leading to a stronger absorbance at the (**) position. To get a quantitative estimate, we have to bear in mind that in this process only the subset of Mn^{2+} ions in the close neighborhood of Yb^{3+} are involved. In section 4.4.4 we have observed and interpreted that the $^4T_{1g}$ energy of this Mn^{2+} subset is lowered by 130 cm^{-1} with respect to the bulk. It is reasonable to assume the same shift for $^4T_{2g}$ and doing so, we calculate an absorbance ratio of 1/3.6 at the positions (*) and (**), respectively. Multiplying with the GSA ratio we obtain 1/29 for upconversion efficiency ratios at 10138 and 10596 cm^{-1}. This compares very favorably with the experimental ratio of 1/38 and confirms the GSA/ESA mechanism.

To separate the GSA and ESA process, we performed an upconversion excitation experiment using two lasers with different wavelengths focused on the same spot at 12 K. The principle of the experiment is shown in Figure 10d. Laser I is fixed at the strong $^2F_{7/2}(0) \rightarrow {}^2F_{5/2}(2')$ absorption of Yb^{3+} at 10596 cm^{-1}. The power of this laser is low (7 mW) in order to minimize one-color upconversion. To probe the ESA step the second laser (II) is scanned between 10 500 and 11 900 cm^{-1} with a power above 100 mW for the whole range. The $^4T_{1g} \rightarrow {}^6A_{1g}$ emission intensity of Mn^{2+} (transition III in Figure 10d) is monitored. The experimental results are shown on the left-hand side of Figure 10. Trace a shows the 12 K one-color upconversion excitation spectrum with only laser II. This is the same as in Figure 9c but scaled up. Trace b shows the result of the two-color 12 K excitation spectrum described above. And trace c shows the $^6A_{1g} \rightarrow {}^4T_{2g}$ absorption band of $CsMnBr_3$:0.5%Yb^{3+} downshifted 10 126 cm^{-1}. The low energy region between 10 555 and 10 800 cm^{-1} the spectrum b matches with a. This is the GSA fingerprint. The new relevant feature in b is the broad excitation band extending from 10 700 to 11 700 cm^{-1}. It is completely absent in (a) and this a result of the second laser (II), which is probing the ESA step Yb^{3+} $^2F_{5/2}(0') \rightarrow Mn^{2+}$ $^4T_{2g}$. Comparison with trace c, which is the $^6A_{1g} \rightarrow {}^4T_{2g}$ absorption band downshifted by 10 126 cm^{-1}, shows similar widths and band shapes and a redshift in (b) of about 140 cm^{-1}. This shift is again associated with the different Mn^{2+} subsets probed in the two experiments. This two-color excitation experiment enabled us to identify and characterize the ESA without contamination by GSA thus provides conclusive proof of the GSA/ESA UC mechanism.

4.4.6. Upconversion Based on Exchange Coupling. The GSA/ESA mechanism as discussed in the literature is a single ion mechanism, whereas in $CsMnBr_3$:Yb^{3+} clearly both Yb^{3+} and Mn^{2+} ions are participating. This situation is similar to the one reported for $RbMnCl_3$:Yb^{3+}.[15] Yb^{3+} ions substitute for Mn^{2+} ions, and in $CsMnBr_3$:Yb^{3+} for the arrangement shown in Figure 1 all Yb^{3+} ions are in close contact (3.26 Å) with a nearest neighbor Mn^{2+} ion through face-sharing octahedra. This close contact provides a pathway for $Yb^{3+}-Mn^{2+}$ exchange interactions. Using the exchange coupled $[Yb^{3+}-Mn^{2+}]$ dimer picture as the simplest approximation of the real situation, we can explain the process as shown on the right-hand side of Figure 12. The ground state of the dimer is denoted $|{}^2F_{7/2}\ {}^6A_{1g}\rangle$. Upon absorption of the first photon around 10 000 cm^{-1}, i.e., the GSA, the intermediate state $|{}^2F_{5/2}\ {}^6A_{1g}\rangle$ is reached, which is essentially localized on the Yb^{3+}. In the ESA step, the second photon is absorbed and the higher excited state $|{}^2F_{7/2}\ {}^4T_{2g}\rangle$ is reached, which is immediately followed by multiphonon relaxation to the emitting state $|{}^2F_{7/2}\ {}^4T_{1g}\rangle$. Both these states are essentially localized on the Mn^{2+}.

With this proposed mechanism we can reconcile the GSA/ESA sequence, which is experimentally well established with the fact that both Yb^{3+} and Mn^{2+} participate in the UC process. The important chromophoric and luminophoric unit is not a single ion but a pair. Whereas the GSA step is still essentially a single-ion excitation on Yb^{3+}, the ESA step requires an exchange mechanism to gain intensity. Such exchange-induced cooperative transitions in mixed transition metal/rare earth systems are not without precedent but they have not been observed in upconversion processes. In Cr^{3+} doped $EuAlO_3$, the R lines in the luminescence spectrum of Cr^{3+} were accompanied by very strong red-shifted lines, and the redshifts were found to correspond to the spinor splittings of the ^7F ground term of Eu^{3+}.[38,39] These cooperative transitions were plausibly ascribed to an exchange mechanism. There is a complete analogy between these transitions and our ESA process, and we thus postulate an exchange intensity mechanism as originally proposed by Tanabe and co-workers[40] to account for our ESA step. In exchange-coupled transition metal ion systems this mechanism can enhance the intensity of formally spin-forbidden transitions by orders of magnitude.[41]

In the title compound the efficiency of the upconversion process, 0.035% at 12 K for 150 mW laser power focused with a lens of $f = 53$ mm, is very low compared to Yb^{3+} doped in $RbMnCl_3$[15] and Rb_2MnCl_4,[42] in which a similar exchange mechanism has been identified. In both these compounds, the UC efficiency is 2 and 3, respectively, orders of magnitude bigger than in the title compound. In $RbMnCl_3$:Yb^{3+} a second Yb^{3+} site was identified, and its UC efficiency is similarly low as in the $CsMnBr_3$:Yb^{3+}. It is plausible that such processes are intrinsically less efficient in bromides than in chlorides. But the above comparison rather suggests an alternative explanation. In Rb_2MnCl_4 all the Mn^{2+} ions are connected by corner-sharing octahedra, in $RbMnCl_3$ both corner-sharing and face-sharing bridging occurs, and in $CsMnBr_3$ there is only face-sharing. It is thus tempting to correlate the high-efficiency and low-efficiency UC processes with corner- and face-sharing $Yb^{3+}-Mn^{2+}$ pairs, respectively. This could account for all the above observations. We hesitate to put this forward as a firm conclusion at this stage. Further work on systems with different bridging geometries, which we are presently engaged in, should clarify the situation.

As seen in trace a of Figure 3 the efficiency of the UC process is reduced by about 1 order of magnitude at 100 K. There are two important loss channels for $^4T_{1g}$ population in the title material. Both are based on excitation energy migration along the chains, which is known to be thermally activated. The first process is intrinsic to $CsMnBr_3$ and independent of Yb^{3+}. It is an energy migration to killer traps, such as Mn^{3+} and Fe^{2+}, which are always present in such compounds. By doping the crystal with Cd^{2+} ions, thus interrupting the chains, the energy migration and thus the losses by these killers could possibly be reduced. We have synthesized and studied such $CsMnBr_3$ codoped with Cd^{2+} and Yb^{3+} and found a similar temperature quenching of the upconversion luminescence as shown in Figure 3a. We attribute this to another loss channel, which is intrinsic to these Yb^{3+} doped octahedral Mn^{2+} systems and cannot be plugged. It is the trapping of the migrating Mn^{2+} $^4T_{1g}$ excitation, by Yb^{3+} ions, either radiatively or nonradiatively. The observation of Yb^{3+} NIR emission upon green Mn^{2+} excitation at temperatures above 40 K (see data in Figure 3c) clearly demonstrates that such a thermally activated process takes place: it is the process shown with double curly/straight arrow on the right-hand side in Figure 12, a transition $[^2F_{7/2}-^4T_{1g}] \rightarrow [^2F_{5/2}-^6A_{1g}]$ in the dimer picture developed in the previous section. Our experimental data do not allow a distinction between a radiative and a nonradiative process. The radiative transitions are exactly of the type as the ESA step in the upconversion process. In the previous section we have argued how such a process can gain efficiency by an exchange mechanism. The nonradiative process is a highly nonresonant energy transfer from Mn^{2+} $^4T_{1g}$ to Yb^{3+} $^2F_{5/2}$ in a single-ion picture. As seen in Figure 2 there is no spectral overlap between the Mn^{2+} $^4T_{1g}$ emission and the Yb^{3+} $^2F_{5/2}$ absorption. We would thus consider it very unlikely. However, if we adopt the Yb^{3+}-Mn^{2+} dimer point of view, it is a multiphonon relaxation between the two dimer states $[^2F_{7/2}-^4T_{1g}]$ and $[^2F_{5/2}-^6A_{1g}]$. In a single ion configurational coordinate picture, these two states are displaced with respect to each other, and the energy difference between their vibrational ground levels is approximately 5800 cm^{-1}. With a phonon cutoff energy of below 200 cm^{-1} in $CsMnBr_3$ a thermally activated multiphonon relaxation across this energy gap appears plausible. This potential loss channel is intrinsic to all Yb^{3+} doped octahedral Mn^{2+} compounds and it prevents the new upconversion process to be efficient at higher temperatures.

5. Conclusions

We report a new type of upconversion process in Yb^{3+} doped Mn^{2+} compounds. After the observation at low temperatures of red Mn^{2+} $^4T_{1g}$ luminescence in $RbMnCl_3$:Yb^{3+} and $CsMnCl_3$:Yb^{3+} upon Yb^{3+} excitation in the NIR,[15,16] the title compound exhibits green and red UC emission bands at 12 K. The green emission is due to a cooperative upconversion luminescence, which has been observed and characterized in many other Yb^{3+} compounds. In the title compound, it happens to lie in an absorption window of $CsMnBr_3$ and thus becomes observable. Of more interest is the red Mn^{2+} $^4T_{1g}$ emission in this and other Yb^{3+} doped Mn^{2+} halide compounds. The present study shows that insight into the mechanisms of this new type of process can be gained by time-resolved and two-laser spectroscopy. The various possible UC mechanisms can be distinguished by their dynamics in the μs to ms time scale, because the potential energy transfer processes are relatively slow. In the title compound as well as in $RbMnCl_3$:Yb^{3+}, it can be established, that energy transfer processes play no important role. Thus both excitation steps in the nonlinear upconversion process are radiative. These steps are individually addressed in the two-color excitation experiments. From their characterization a relatively clear picture of the upconversion mechanism arises. It is a sequence of GSA and ESA steps. But the ESA step does not take place on a single ion, as is usually the case in rare earth systems. It requires exchange coupling between neighboring Yb^{3+} and Mn^{2+} in the lattice, and in the simplest picture we consider the $YbMnBr_9^{4-}$ dimer consisting of face-sharing octahedra as the relevant chromophoric unit. In transition metal and mixed TM/RE systems exchange interactions play a much more important role than in pure RE systems. The combination of TM and RE ions in the same crystal thus opens new pathways for upconversion with exciting new results.

Acknowledgment. The authors are grateful to Stephan Heer and Markus Wermuth for helpful discussions on upconversion and their constant interest in this work and Karl Krämer and Patrick Reber for their help with crystal growth. The Swiss National Science Foundation is acknowledged for financial support.

IC010081F